Development and Calibration of a new Anechoic Wall Jet Wind Tunnel

Austin Kleinfelter[1], Russell Repasky[2], Nandita Hari[3], Stefan Letica[4], Vidya Vishwanathan[5], Lee Organski[6], Jonathan Schwaner[7], W. Nathan Alexander[8], and William Devenport[9]
Center for Renewable Energy and Aerodynamic Technology. Virginia Tech, Blacksburg, VA, 24061

A new Anechoic Wall Jet Wind Tunnel was built at Virginia Tech. A detailed design based on the old wall jet tunnel was done to improve the quality of the resultant flow. Aerodynamic and acoustic calibrations were performed in order to understand properties and characteristics of the flow generated by this new facility which can be used for various aeroacoustic studies. Far-field acoustics were measured using half-inch B&K microphones in a streamwise array to characterize and reduce the background noise. Sound pressure levels were lower by 10 dB for frequencies up to 700Hz in comparison to the old facility. The turbulent surface pressure fluctuations of the wall-jet flow were studied using Sennheiser microphones placed along streamwise and spanwise locations to record surface pressure fluctuations. Comparison of the autocorrelation plotted for microphones along the same span indicate uniform flow features. A decay in the turbulence levels is observed along the downstream direction as expected. Aerodynamic calibrations included mean velocity measurements along different spanwise locations, wall-jet boundary layer profiles and streamwise cross-sections. Spanwise and cross-sectional velocity profiles show good uniformity of the flow. Detailed boundary layer analyses were performed with the parameters obtained from the experiments.

I. Introduction

The anechoic wall-jet wind tunnel has become an important tool in the study of noise generated by surface flows. The wall jet arrangement allows a relatively high-speed flow to be generated over a surface at laboratory scale with no significant edge noise sources and with a jet boundary that allows for both an anechoic environment and for microphones to be placed outside the flow. As a result, this configuration has been instrumental in recent years in providing experimental insight into roughness noise sources (Grissom 2007, Smith 2008, Alexander 2009, Glegg *et al.* 2009, Alexander 2011, Devenport *et al.* 2011, Alexander *et al.* 2013, 2014, Devenport *et al.* 2018), noise generated by boundary layer flows over embedded steps (Jacob *et al.* 2001, Catlett 2010, Awasthi 2012, Awasthi *et al.* 2013, Awasthi *et al.* 2014, Catlett *et al.* 2014, Awasthi 2015), flows over acoustically treated surfaces for wind tunnels (Alexander *et al.* 2014, Alexander *et al.* 2015), acoustics of canopy flows (Clark *et al.* 2014, Clark *et al.* 2016, Clark 2017) and a novel approach to the measurement of surface pressure wavenumber spectra using an acoustic diffraction grating (Devenport *et al.* 2010). Much of this experimental data originated in the Virginia Tech Anechoic Wall Jet Wind Tunnel – a facility built as a temporary structure in 2007. This paper describes an effort to build a new facility to this design with both enhanced acoustic and aerodynamic qualities. This facility, replacing the old wall jet tunnel, will continue efforts to understand the aeroacoustics of flow over surfaces, with a new study to research applications of metasurfaces, aeroacoustics, etc.

---

[1] Graduate Research Assistant, Department of Aerospace and Ocean Engineering
[2] Graduate Research Assistant, Department of Aerospace and Ocean Engineering
[3] Graduate Research Assistant, Department of Aerospace and Ocean Engineering
[4] Graduate Research Assistant, Department of Aerospace and Ocean Engineering
[5] Graduate Research Assistant, Department of Aerospace and Ocean Engineering
[6] Undergraduate Research Assistant, Department of Aerospace and Ocean Engineering
[7] Undergraduate Research Assistant, Department of Aerospace and Ocean Engineering
[8] Assistant Professor, CREATe, Department of Aerospace and Ocean Engineering
[9] Director, Virginia Tech Stability Wind Tunnel, Department of Aerospace and Ocean Engineering

Virginia Tech's original anechoic wall jet facility measured and characterized the far-field noise of turbulent airflows over various rough surfaces. Data provided from Grissom (2007) was used to develop predictive models of roughness noise. Unfortunately, the structural integrity of this facility began to deteriorate due to extensive use and poor structural fabrication techniques. Therefore, the design and construction of a new anechoic wall jet facility ensued in 2017. This facility was constructed with more advanced materials, laying the framework for a significantly improved operational life. Additionally, the anechoic chamber is larger, allowing for easier experimental setup. A wall jet is characterized by a high-aspect-ratio rectangular exhaust flow onto a flat plate. For this design, the lower nozzle of the exhaust blends fluidly into the flat plate, generating an attached flow with no added edge noise. This is shown in Fig 1. Wall jets consist of two main flow regions: the outer mixing layer and inner boundary layer. The inner boundary layer consists of the region near the wall, below the point of maximum velocity in the wall-jet profile. The wall jet profile is nearly self-similar as shown by Grissom (2007). The flow velocity gradually decreases with distance from the nozzle but remains uniform across the span of the plate, with near-perfect symmetry across the nozzle centerline. Basic flow measurements of the wall jet therefore provide well-defined characterization of the boundary layer and its development with distance from the nozzle, a necessity for aeroacoustics modelling. This study reports on the design and acoustic and aerodynamic calibration of the new anechoic wall-jet facility at Virginia Tech.

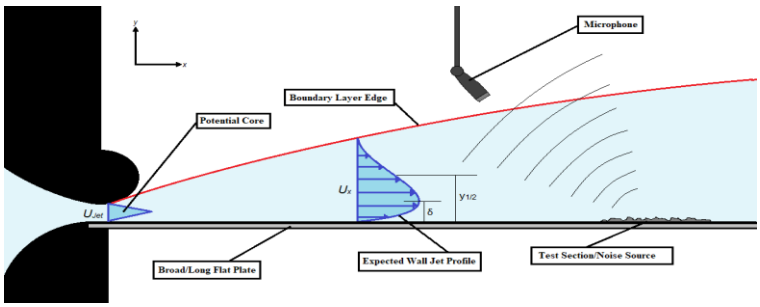

Fig 1. *Diagram showing boundary layer growth over a typical wall jet*

II. Tunnel Design

A. Selection and Installation of Blower

A Cincinnati Fan model HP was selected for the operation of the original wall jet. It was determined that the original unit was sufficient for the operation of the new facility. The fan can produce a maximum volumetric flow rate of 0.945 m^3/s and was equipped with a SSA-8 steel discharge silencer, reducing broadband noise by 5 to 10 dB. In the 2007 tunnel configuration, the silenced blower could produce exhaust velocities at the nozzle of up to 60 m/s.

B. Settling Chamber Design

In a standard wind tunnel design, there is a diffuser section after the flow generation source. The diffuser acts to increase the cross-sectional area of the flow while minimizing separation along the walls. In the original facility, the flow exhausted from the ducting, and cascaded downwards into an open cavity of the settling chamber. This effectively creates a pressure chamber. Settling chambers typically straighten flows that become disorganized from wide-angle diffusers, and control boundary layer effects through different treatment methods. These treatment methods are typically in the form of honeycomb cell structures for flow straightening, and gauzy mesh screens for boundary layer treatments (and some flow straightening).

The priority of the settling chamber in the anechoic wall jet was to block the acoustic line of sight from the blower inlet to the nozzle, isolating the test section from any blower noise as much as possible. This was achieved in similar fashion as the previous tunnel design, by passing the flow through a labyrinth of acoustically treated center and side panels. This increases the number of reflections required for sound to reach the nozzle, giving more chances for diffusion by the foam. The configuration of the baffles was kept in the optimized form developed in the original tunnel design from Grissom (2007). This chamber is internally 2108 mm long, 1152 mm wide, and 1181 mm tall. It is filled with two sets of baffles that reach floor to ceiling. The center section

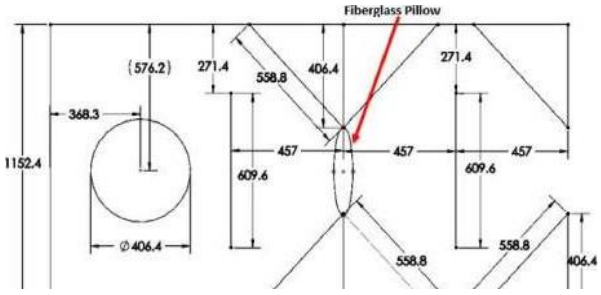

Fig 2. *Internal drawing of settling chamber. The circle, left, is where the air enters the chamber from the blower, and the small gap, right, is where the flow exits into the nozzle chamber. The red arrow points to a 100mm fiberglass pillow.*

is 609.6 mm wide and the sides extend 406.4 mm into the flow.

A major difference between the internal construction of the current settling chamber and that of the old design was the inclusion of MDF slopes on the up and downstream portions of the side pieces. This generates less turbulence in the flow as it travels through the acoustic labyrinth. In the previous design, there were places for the slow-moving

1/3 Octave Center Freq (Hz)	125	250	500	1000	2000	4000
Absorption Coefficient	0.28	0.39	0.74	0.69	0.75	0.96

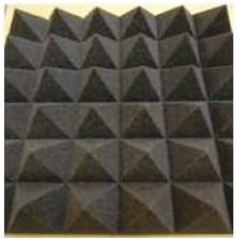

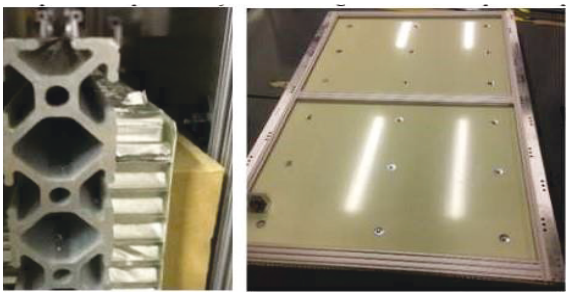

Fig 3. *Above Left: Absorption coefficient Vs. test frequency in a Reverberation Room Method Test. Below Left: A picture of the 4 in Acoustic pyramid foam procured from Foam Factory. Middle: Left- Side view of wall composition. From right to left: 19.05 mm MD.*

air to gather and create large eddies. A 2D view of the internal layout is provided in Fig 2. All surfaces of the settling chamber were treated with 101.6 mm acoustic pyramid foam from Foam Factory. This foam was chosen as a decent compromise between absorption and price. A picture of the foam and a range of acoustic absorption coefficients are provided in Fig 3.

The most impactful change of the new project was the wall construction of both the settling and nozzle chambers. A major problem with the previous tunnel was the incapacity of the purely MDF construction to handle the pressure required at the higher velocity ranges. This led to large deflections of the sidewalls and ceiling during operation, causing the caulk in the joints to stretch and break over time allowing large pressure losses. As the velocity is directly tied to the dynamic pressure of the settling chamber to the outside air, these leakages prevented the tunnel from operating at optimum conditions. To correct this, a wall composition was chosen that combines the acoustic dampening properties of MDF with the high flexural rigidity provided by aluminum honeycomb.

C. Contraction Section Design

The new nozzle section chamber was constructed using the same updated wall composition as the settling chamber. This section is a bit larger than the settling chamber to ensure that the nozzle width will remain the same as the previous tunnel. The inner dimensions of this section are 1244.85 mm tall, by 1206.75 mm long, by 1029.59 mm long. The goal of this section is to compress the flow into the 12.7 mm high nozzle slit with as little disturbance to the air as physically possible. This was achieved using an equation which was originally obtained from Fang (2001). The cubic equation is optimized to be the most effective shape for a non-separating flow contraction. The general equation for the contraction slope is given in Equation 2.1 obtained from Fang (2001).

$$y = (h_1 - h_2)[1 - 1/X_m^2(x/L)^3] + h_2, for x < X_m$$
$$y = (h_1 - h_2)/(1-1/X_m)^2(1-x/L)^3 + h_2, for x > X_m \quad (2.1)$$

In the above equation, x and y indicate the points of the contraction slope where y is defined perpendicular to the flow while x is parallel. L, h_1, and h_2 are the length of contraction, the chamber half height, and the half height to the opening of the nozzle respectively. X_m is adjustable to the curve desired and defines the inflection point of the final cubic curve.

One of the major changes for the nozzle section in the redesign was the inclusion of a full contraction slope on the upper part of the nozzle. This addition was possible due to the fixing of the nozzle at 12.7 mm as discussed in Clark (2014). Contraction slopes flanking the top and bottom of the section provide more uniform flow with less noise and pressure loss as shown by Clark (2014). Each contraction slope was defined with individual values for the inflection point to fit within the chamber appropriately and provide the smoothest transition onto the nozzle.

The upper and lower contraction slopes were shaped using six 19.05 mm thick MDF supports each. These supports were milled with precision by the department machine shop. Sheets of 3.175 mm PVC were mounted and attached with countersunk screws and smoothed using Bondo Filler and Resin produced by 3M. The contraction slopes were

then sanded using very fine grit sandpaper and sealed with Novus No.2 Fine Scratch Remover. Additionally, the connection between the slopes and the sidewalls was sealed with a bead of clear silicon caulk. Both the top and bottom nozzle blocks were milled from one piece of Raku Tool model MB-0720, Polyurethane Board. This was chosen over PVC because the material maintained the smooth surface structure required to prevent flow separation. The polyurethane also allows the entire nozzle block to be milled in one piece, preventing problems observed in the previous facility such as joint separation over time. A side view of the contraction slope is shown in Fig 4.

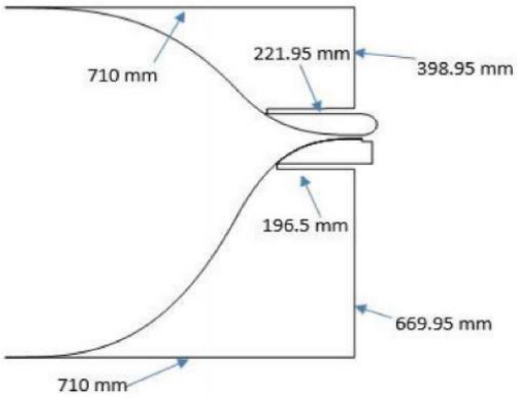

Fig 4. *Simple Diagram of contraction slopes and extended nozzles defined by the cubic function discovered by Fang (2001). Gaps between the slopes and nozzles allow for lengthwise MDF panels facilitating secure attachment of the nozzle pieces.*

D. Anechoic Chamber

The first consideration in the new anechoic chamber was space around the testing location for ease of movement during model set up. This also creates more room for instrumentation and the possibility of a 3D motor driven traverse. Aluminum was chosen for the framing to minimize both cost and weight as the large 4.718 m long, 3.238 m wide, and 2.744 m tall chamber was intended to be rolled away from the plate if necessary. The wall panels were chosen as 19.07 mm thick MDF to minimize cost and maximize sound absorption from both inside and outside the enclosure. The panels were painted with a viscoelastic material to further increase density and sound absorption. This material was Rustoleum Truck Bed Coating Spray. The entire inside of the anechoic chamber is covered in 101.6 mm acoustic wedge foam and 152.4 mm square bass corner foam purchased from Foam Factory. These were chosen to absorb high frequency sound from the jet and edge noise while minimizing cost. Figure 5 shows the two types of foam and absorption data for the wedge foam provided by the manufacturer. The height of the acoustic shelf above the jet was selected as 229 mm from the flat plate. The shelf was maintained at the orientation specified in Clark (2014), with a 300 mm gap in front of the shelf to allow reclamation of air in the jet, creating a smoother flow. The shelf is 589 mm wide. It was framed using 2x4's, then wrapped in 19.07 mm MDF and acoustic wedge foam. The wedge foam on the bottom of the acoustic baffle is oriented in the streamwise direction. This prevents any interference of laterally oriented edges on the uniformity of the upper sections of the boundary layer. Figure 6 shows an internal side view of the anechoic chamber giving the relevant technical dimensions.

1/3 Octave Center Freq (Hz)	125	250	500	1000	2000	4000
Absorption Coefficient	0.39	0.61	0.91	0.79	0.95	1.03

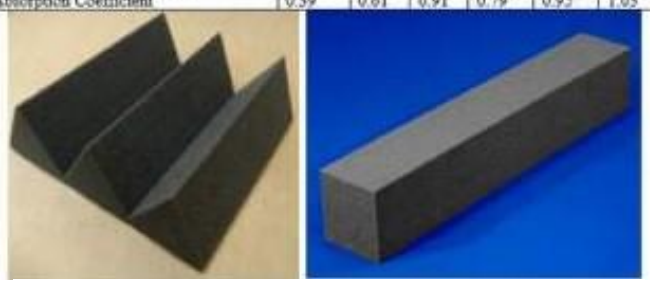

Fig. 5: *Above: Absorption coefficient Vs. test frequency in a Reverberation Room Method test. Below Left: A picture of the 101.6 mm Acoustic wedge foam procured from Foam Factory. Below Right: A picture of 152.3 mm square bass corner foam from Foam Fact.*

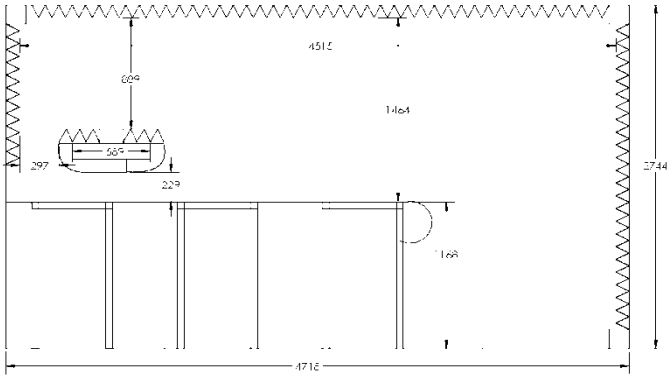

Fig. 6*: Side view drawing of anechoic chamber around test plate. 159 mm high casters not shown. All dimensions in mm. All walls, ceiling, and baffle covered in 101.6 mm acoustic wedge foam, corners filled with 152.4 mm acoustic square bass foam. Floor covered in 101.6 mm acoustic wedge foam, corners filled with 152.4 mm acoustic square bass foam. Floor covered in 457 mm acoustic wedges.*

E. Test Plate

The flat plate, or wall, in the new wall-jet facility was directly transferred from the old tunnel as there were no defects sustained during the years of operation. The steel stand design was also retained due to the larger anechoic chamber removing many concerns of testing area accessibility. The wall was fabricated with high precision by Kaiser Aluminum and is made of Aluminum 6061-T651. The plate is 3048 mm long, 1524 mm wide, and 9.525 mm thick. The bottom surface of the wall is held 1333.5 mm above the floor by a 3-piece steel frame. The three steel frames used to support the wall were each 610 mm long and 1830 mm wide. The steel used was 50.8 mm box tubing with a 1.5 mm wall thickness. Extra-long bolts were used to bolt the frames to the floor, with adjustable feet to lock them in place, removing any chance of the plate changing position over time. The plate itself was made of 3 different pieces, each bolted together in numerous places along the seams. The seams were then sealed with aluminum tape to ensure a smooth flow. A top view of the wind tunnel is shown in Fig 7.

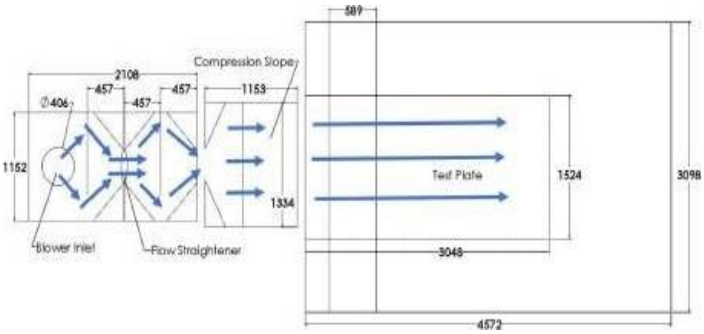

Fig 7. *Top view of entire facility excluding the blower enclosure, with general flow directionality shown by blue arrows. All dimensions in mm.*

III. Instrumentation and Experiment

A. Acoustic Calibration

The primary purpose of the new anechoic wall jet facility is to characterize the aeroacoustics of flow over various surface and edge geometries. Due to the sensitive nature of acoustic levels near the testing region, it is crucial that the background noise of the facility is as low as possible. Therefore, a calibration scheme is needed to measure the far-field region to optimize acoustic performance. To accomplish this, Brüel & Kjær (B&K) Type 4940 ½ inch microphones were placed in a streamwise arc above the centerline of the test plate as shown in Fig. 8. An individual Type 4940 microphone is shown in Fig. 9. These microphones were used because they have desirable dynamic and frequency ranges for measuring the far-field levels. These ranges are 14.6-146 dB and 6.3-20000 Hz respectively. The general sensitivity of the microphones is 50mV/Pa. Each B&K ½ inch microphone is equipped with a factory-made salt-and-pepper cap to protect the diaphragm. Two configurations were used: six microphones with an arc radius of 609mm, and five microphones with an arc radius of 813mm. Diagrams for these setups are shown in Fig. 10. The latter only has five microphones because the support gantry was not long enough to hold the furthest downstream microphone. The microphone placements were designed to emulate far-field testing arrangement of the old wall jet facility, as seen in Clark (2015), to compare facility performances. Each microphone was oriented to face the center point of the test plate using an alignment laser. Angles were measured using an inclinometer and an aluminum square as a datum. Acoustic measurements were made with a completely smooth test wall, any seams or other features covered with hydrodynamically smooth 40-micron tape. Microphones underwent a pistonphone calibration at 251.2 Hz to determine their sensitivities. A high-pass filter of 22.4 Hz was applied to the measurements. Sound measurements were made for jet exit velocities of 20 to 70m/s in increments of 10m/s. Measurements were made for for 60s, at a continuous sampling rate of 65536 Hz. The analog signal from each microphone was digitally converted using a B&K Type 3050-A-060 DAQ. The data was collected on a laptop using the B&K Pulse Time Data Recorder Software. It was then post-processed using an in-house MATLAB code.

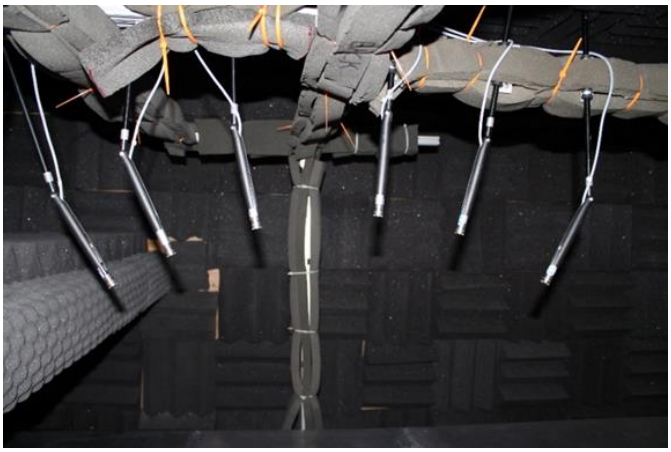

Fig. 8: *Streamwise array of B&K ½ inch microphones arranged in an arc-like sketch to capture background noise contamination around the wall jest testing area. The 609mm radius setup is shown.*

Fig. 9: *A B&K Type 4940 ½ inch microphone used in the streamwise array to measure the wall jet background noise. Shown equipped with a factory-made salt-and-pepper cap to protect the diaphragm.*

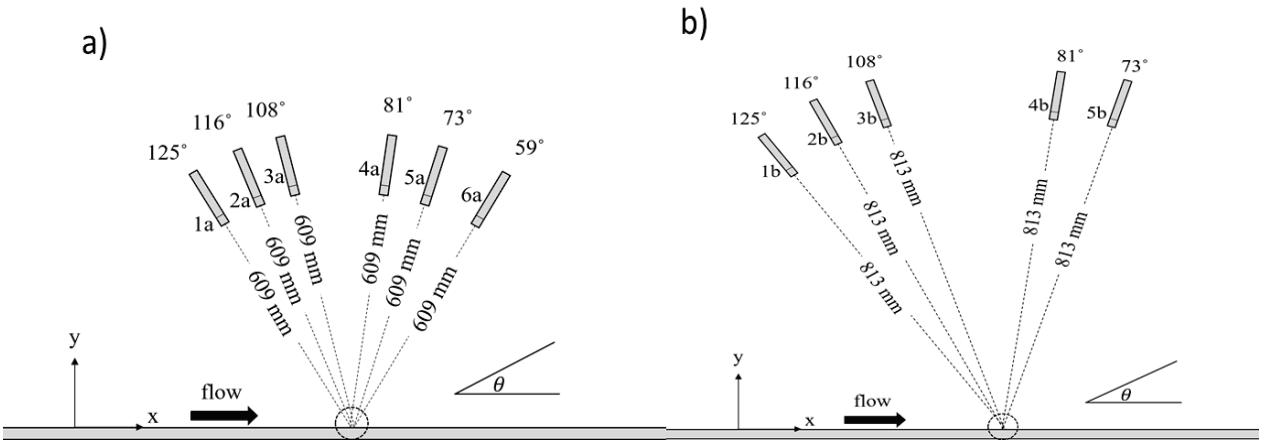

Fig. 10: *Diagrams of the microphone setup used to measure background noise surrounding the test plate center. The microphones are labeled 1-6. The center is shown using the dashed circle. The diagram on the left displays the 609mm radius setup (setup A) while the diagram on the right displays the 813mm radius setup (setup BF). Dimensions are not to scale.*

B. Surface Pressure Measurements

Turbulence of the wall jet air sheet was studied using microphones to measure the fluctuating pressure spectrum on the wall. Sennheiser KE 4-211-2 microphones were selected to measure said spectra because of their fine sensitivity, 10mV/Pa, and small 1-mm pinhole, Fig. 11. This provides a greater resolution of small-scale eddies oscillating. The frequency range of the microphones is 20-20000 Hz. The measurement setup consisted of five microphone placements in the test wall spanning the test plate in both the streamwise and spanwise directions, Fig. 12. Care was taken to ensure that the Sennheiser microphones were mounted flush to the wall surface. 40-mircon tape was used to cover any surface irregularities around each microphone pinhole, without interfering with the pinhole itself. Each Sennheiser microphone was calibrated using a pistonphone at 251.2 Hz to determine its sensitivity. A high-pass filter of 0.7 Hz was also applied to the measured signals. Tests were run using six flow velocities, 20-70m/s in increments of 10m/s. The surface pressure fluctuations were measured for 32s, with a sampling rate of 65536 Hz. The analog signal from each microphone was digitally converted using a B&K Type 3050-A-060 DAQ. The data was collected using the same software as the far-field microphones, and post-processed using

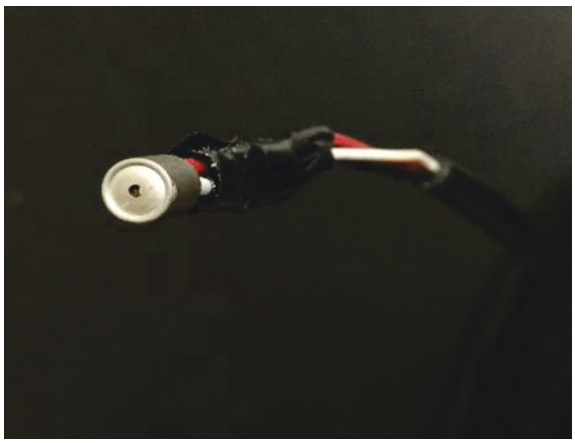

Fig. 11*: A Sennheiser KE 4-211-2 microphone with the 1mm exposure hole.*

an in-house MATLAB code. Autospectral data was obtained by rotating a single microphone over each of the five positions per velocity sweep.

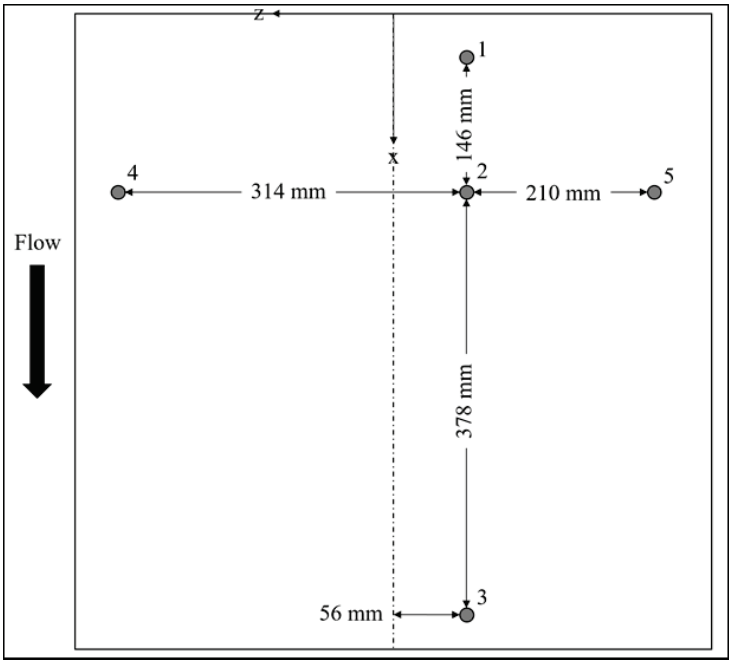

Fig. 12: *Diagram of surface pressure microphone placements on the 610x610mm test plate area. The locations are labeled 1-5. The locations near the ends of the test plate are 43 mm from their respected edges due to underlying 80x20 support pieces.*

C. Aerodynamic Calibration

The aerodynamic performance and calibration of the facility is equally important as the acoustic performance. To ensure that the flow is uniform, the mean velocity was measured at a number of different streamwise locations across the span within the boundary layer. The tests performed include spanwise velocity profiles, a wall-jet boundary layer analysis, and streamwise velocity cross-sections. The spanwise velocity profile and streamwise velocity cross-sections demonstrate the uniformity of the jet at multiple downstream measurement locations. The desired performance is uniform flow across the spanwise width of the test plate at a minimum, maintained along the streamwise length of the test plate.

i. Nozzle Exhaust Uniformity

The first step in determining the flow characteristics of the new tunnel was to ensure uniform velocity across the nozzle. To achieve this measurement, a rig was constructed which would hold a long pitot probe inside the nozzle at the point of closest convergence with the plate. The test rig with the pitot probe at the nozzle and the pitot probe itself are shown in Fig 13. The rig had the capability to measure the velocity at 5 spanwise locations. The pitot probe was attached to an aluminum angle mounted on stands that kept it out of the flow both vertically and laterally. This pitot probe was attached to 3.175 mm inner diameter tygon tubing which was fed into two transducers. The first transducer measures the difference in pressure between the pitot probe and the pressure taps in the settling chamber, while the second measure the

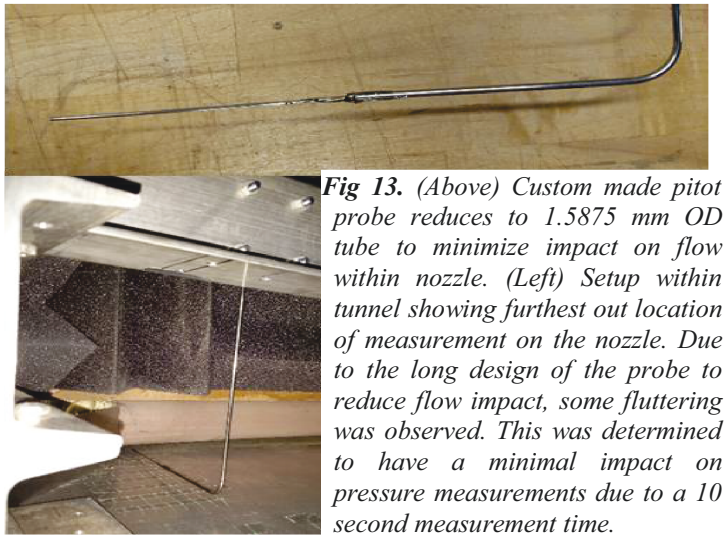

Fig 13. *(Above) Custom made pitot probe reduces to 1.5875 mm OD tube to minimize impact on flow within nozzle. (Left) Setup within tunnel showing furthest out location of measurement on the nozzle. Due to the long design of the probe to reduce flow impact, some fluttering was observed. This was determined to have a minimal impact on pressure measurements due to a 10 second measurement time.*

dynamic pressure between the probe an ambient pressure tube located underneath the table in the chamber. The ambient pressure tap is located 1.524 m downstream of the nozzle and well underneath the table to ensure an accurate no flow measurement.

ii. Span-wise Flow Uniformity

As with the acoustic measurements, the desire for the new anechoic wall jet facility was to demonstrate aerodynamic performance equal or better to that of the old facility. Before applied testing could be performed in this facility, it was important to understand and document its aerodynamic performance.

As discussed above, wall-jet flows typically exhibit a high level of uniformity across the span. Both Grissom (2007) and Clark (2014) performed tests to document the span-wise uniformity of the flow, and to highlight any problems that caused non-uniformities. The performance of the new facility was assessed by using a flattened-head Pitot probe on a two-dimensional traverse, identical to that used by Clark (2014). The detailed dimensions of the test probe, as well as its orientation used for data acquisition, is shown in Fig 14. The traverse configuration in the test chamber is shown in Fig 15. Dynamic pressures were measured between the settling chamber and ambient pressure, and the Pitot and ambient pressure. Data acquisition was conducted using an in-house developed MATLAB program to control the traverse and record pressure measurements. Flow velocity was measured using the flattened-head Pitot probe manufactured in-house. To support the probe, a metal frame was placed on the plate which consisted of two 6.4 mm base plates spaced 1.32 m from edge to edge. The vertical support structures attached to these base plates were spaced 1.44m apart. These supports were spaced such that the supports would remain outside the main region of flow. A cross-bar ran between the two vertical supports, such that the bottom of the cross-bar was elevated 216 mm above the plate. This allowed a majority of the flow to pass beneath the cross-bar unhindered. The 2-D traverse, powered by two Compumotor 557-83-MO stepper motors connected to threaded rods which were in turn connected to a metal bracket, rested on the cross-bar. Finally, a 3.2 mm diameter rod was held vertically by this metal bracket and extended below the cross-bar. A right-angle bracket was used to connect this vertical rod with a similar 3.2mm diameter rod oriented horizontally to which the Pitot probe itself was attached. In this configuration, the two stepper motors could control the vertical and spanwise movement of the Pitot Probe. The streamwise position of the traverse was set manually by moving the entire structure.

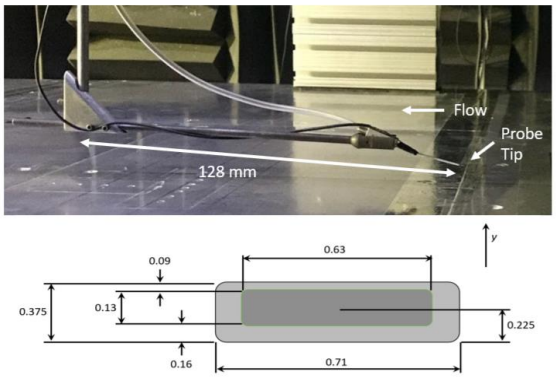

Fig 14. *(Above) Pitot probe mount positioned with the probe tip just touching the test plate. (Below) Detailed dimensions of the pitot probe in mm.*

The Pitot probe was attached to 3.175 mm inner diameter tygon tubing which was fed into a pressure transducer. The ambient pressure was measured using 3.175 mm inner diameter tygon tubing placed under the table 1.524 m downstream of the nozzle. The flow speed at the nozzle exit was determined using 3.175 mm inner diameter tygon tubing taps in the settling chamber against the ambient pressure inside the test chamber. The pressure transducers were both connected to an NI DAQ which allowed an in-house MATLAB program to measure jet velocity and local velocity simultaneously. Mean velocity data was calculated using the average of 50 records containing 1024 data points sampled at 6400 Hz. This resulted in a total measurement time of 8 seconds. As part of the in-house program, a time buffer was used between measurements to ensure that the probe had finished traversing before recording measurements.

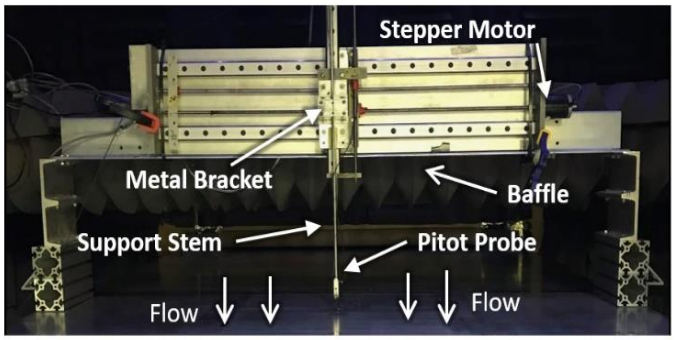

Fig 15. *2-D Traverse capable of moving in the z (horizontal) and y (vertical) axes with labeled components.*

In order to detect contact between the plate and the probe, an electrical circuit was set up which would be closed upon contact with the metal plate. A digital multimeter was used to measure the resistance in the circuit. Spanwise

flow measurements were recorded 6.35 mm off the wall at streamwise locations of 0.9779 m, 1.1557 m, 1.3081 m, 1.4605 m, and 1.7653 m downstream of the nozzle and for flow speeds at the nozzle of 30, 40, 50, 60, and 70 m/s.

iii. Boundary Layer Measurements

In order to fully characterize the flow in the tunnel, vertical velocity profiles were measured at the same streamwise locations presented above for the spanwise measurements. As for the spanwise measurements above, the position, reference velocity, ambient temperature, dynamic pressures, and ratio of local to jet velocity were recorded starting at the wall up to a vertical height of 152.4 mm. To relate these discrete measurements to flow throughout the tunnel, some knowledge of the development of the flow structure is necessary. Wygnanski *et al.* (1992) describe velocity measurements performed on a different wall-jet facility to analyze the development of the flow as it moves over a flat plate. They found that the "law of the wall" applies only to the viscous sublayer for wall-jet flows, but also state that the "law of the wake" can be applied to the inner region of wall-jet flows. Most importantly, they developed several formulations to relate the maximum velocity in the boundary and the boundary layer thickness to non-dimensional flow properties using the fact that the boundary layer profiles were self-similar once the flow was fully developed. Slightly modified versions of these equations were used to allow for the full characterization of flow development in the wall-jet facility presented here. These equations will be presented along with details of the analysis performed in the Results and Discussion.

IV. Results and Discussion

A. Acoustic Calibration

The goal of taking far-field acoustic measurements was to characterize the parasitic background of the tunnel. Figure 16 shows the power spectral density of the signal measured by the microphone array shown in Fig. 10a. Figure 16a displays the measurements of microphone 1a as a function of jet velocity, while Fig. 16b shows the measurements of all microphones in setup A at $U_{jet} = 70m/s$. To process the time series data, a MATLAB function was used to perform a fast Fourier transform of the data sectioned into records of length 8192 with overlap 50%. Furthermore, a periodic Hanning window was used to weight the data of each record correctly. Each spectrum was sorted into 12 logarithmically spaced bins per octave to smooth the curves. The normalized spectra are then plotted as 1Hz bandwidth SPL (sound pressure level).

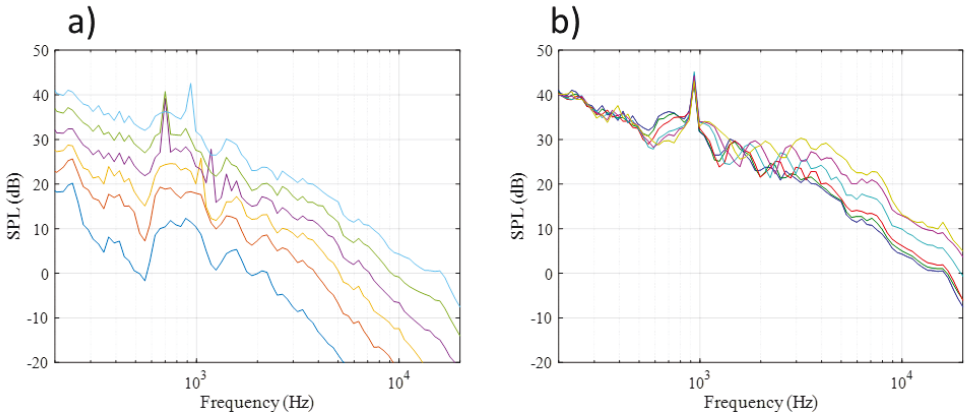

Fig. 16: *Plots displaying the background noise levels measured using microphone setup A. Figure 6a displays data from mic 1a at $U_{jet} = 20m/s$ (—), 30m/s (—), 40m/s (—), 50m/s (—), 60m/s (—), and 70m/s (—). Figure 6b displays data at $U_{jet} = 70m/s$ for mic 1a (—), mic 2a (—), mic 3a (—), mic 4a (—), mic 5a (—), and mic 6a (—).*

The spectra show a general reduction in level from low to high frequency, with an interruption of the trend between 700 and 1050 Hz. Of note is the spike in frequency at around 700 Hz that begins to dominate the signal at jet speeds of 50 m/s. This tone was audibly confirmed by the research team to originate from the tunnel's contraction chamber and flexing the walls of the chamber changed the tone. As expected, the tone frequency increased as the jet speed increased. The SPL values also increase with increasing jet velocity, growing by an average of 5 dB with a U_{jet} increase of 10m/s. As expected, the far-field noise at downstream observer angles is greater than that at upstream

angles, with a difference of around 12 dB between the 125° and 59° microphones. This is due to the better shielding of the upstream microphones from the wall jet nozzle by the horizontal baffle seen in Fig. 8.

To further explore the effects of the horizontal baffle, the plots in Fig. 17 were produced from the data taken from the setup in Fig. 10b. Here it can be seen that the dominant frequency spikes begin at 40 m/s instead and are at a higher frequency than the spikes seen in setup A, although the general shape of the spectra remains. The shifting in these spikes could be due to differing conditions in the tunnel, since the data were not recorded sequentially, but nonetheless, they are indicative of an upstream leak in the contraction chamber. The SPL levels increase with increasing jet velocities and decrease with downstream position in a similar manner as in setup A.

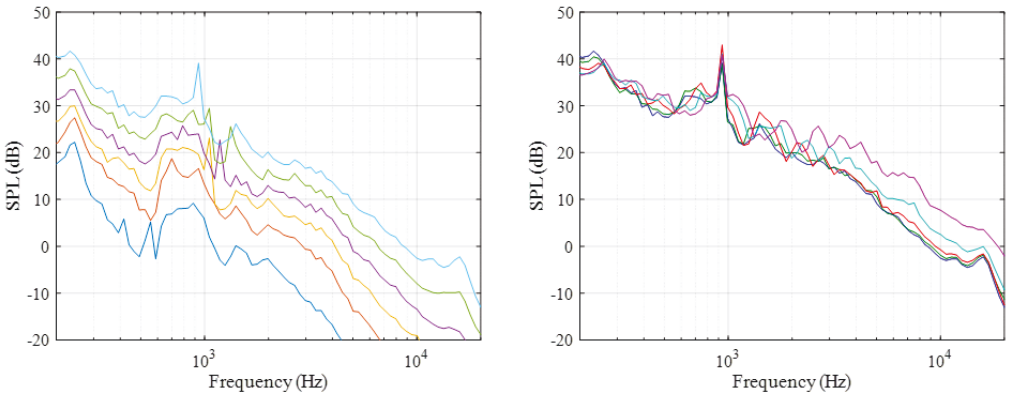

Fig. 17: *Plots displaying the background noise levels measured using microphone setup B. Figure 7a displays data from mic 1b at $U_{jet} = 20m/s$ (), 30m/s (), 40m/s (), 50m/s (), 60m/s (), and 70m/s (). Figure 7b displays data at $U_{jet} = 70m/s$ for mic 1b (), mic 2b (), mic 3b (), mic 4b (), and mic 5b ().*

To properly compare the performance between both far-field setups, it is desirable to scale each to a common observer location relative to the center of the test plate. An observer distance of 1m was selected, and the comparison can be seen in Fig. 18. Figure. 18a shows the setup comparison at the 125˚ location while Fig. 18b shows the analysis at the 73˚ location. Each plot shows a general decrease in the SPL levels using the data from setup B, with exception to the lowest frequencies at the 73˚ location. The stronger performance of setup B is apparent in the microphones at 125˚ and is expected because of its location deeper into the baffle configuration. This provides increased protection from noise resonating from the nozzle. This noise reduction is also shown at frequencies above 4000 Hz at the 73˚ location. The improved performance of setup B makes it a desirable option for future testing.

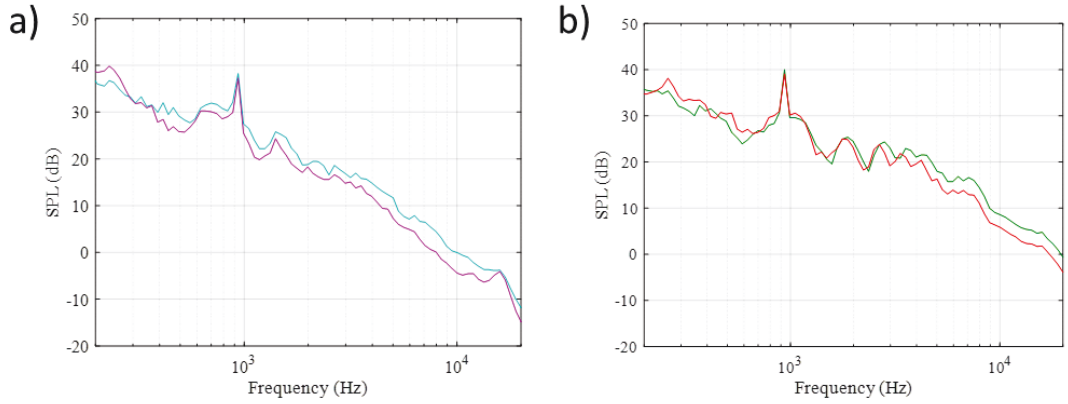

Fig. 18: *Plots comparing the relative SPL levels between far-field microphone setups A and B corrected to an observer distance of 1m from the center of the test plate at $U_{jet} = 70m/s$. Figure 8a displays mic 1a () and mic 1b (). Figure 8b displays mic 5a () and mic 5b ()*

In Fig. 19, a comparison is drawn between data recorded by Clark (2015) in the previous Virginia Tech wall-jet facility and data recorded using setup B by the current research team in the new facility for an observer angle of 125°, shown in Fig. 17. SPL levels have been corrected to an observer distance of 0.6m, using the distance from the center of the test plate. This distance was selected to remain consistent with data reduction from the previous facility. In these terms, compared to the old facility, the new facility produces 10 dB less noise at frequencies up to around 700 Hz. This is ideal, as it means that in the new facility, low-frequency noise applications can be studied. After 700 Hz, at high frequencies the new facility is over 10dB louder at the lowest flow speed, but has almost the same background levels at 70m/s.

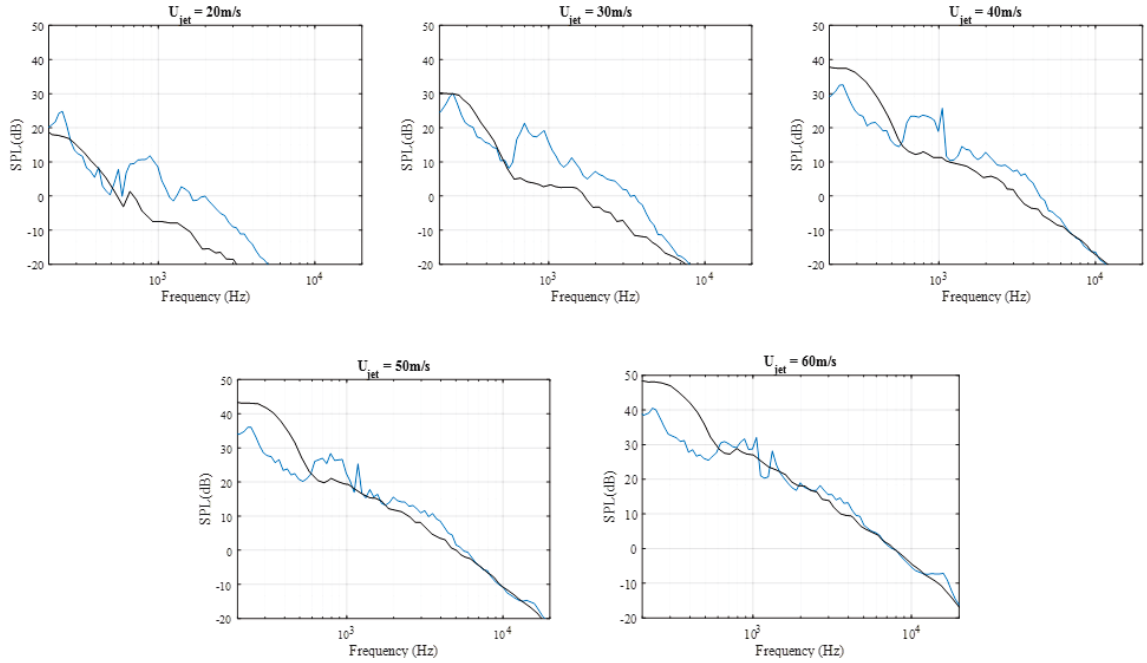

Fig. 19*: Plots comparing the background noise between the old facility (▬) and new facility (▬) at five different jet velocities. Both facilities are corrected to an observer's distance of 0.6m from the center of the test plate.*

B. Surface Pressure Measurements

The wall pressure spectra at five different streamwise and spanwise locations was measured at velocities of 20m/s to 70 m/s in increments of 10m/s. Figure 20 compares the autospectra data measured at the three streamwise locations with the 1Hz bandwidth Sound Pressure Level (SPL) on the vertical axis plotted against frequency in the horizontal axis. The spectra in general shows higher amplitude fluctuations at the low frequency range (below 1 kHz) which are likely due to the large scale and high energy structures present in the outer mixing layer. Mid frequency ranges typically showed similar slopes at all tested flow speeds. The high frequency range showed a rapid decrease in the spectral levels which can be related to a typical energy cascade of turbulent boundary layers and viscous dissipation of the smallest turbulent scales in the flow. The frequency range has been truncated to remove the noise floor and measurements below and above the useable frequency range. With increase in flow speed, there is an increase in the pressure fluctuation levels observed indicating higher energy associated with larger flow speeds. A shift in the frequency can be observed with increasing flow speeds due to an increase in the convective velocities of the turbulent structures causing the pressure fluctuations.

The streamwise line of microphone positions shows a consistent trend for all flow speeds. The sound pressure levels and frequency of pressure fluctuations can be observed to reduce with downstream distance. This can be attributed to the reducing energy levels as the flow moves downstream. Figure 21 shows the sound pressure levels plotted at three microphones placed along the spanwise direction. The autospectra plotted for all the mics collapse well for different flow speeds, confirming the two-dimensionality of the flow here. The sound pressure levels increase for all three mics with increasing flow speed. Slight deviations at higher frequencies can be observed.

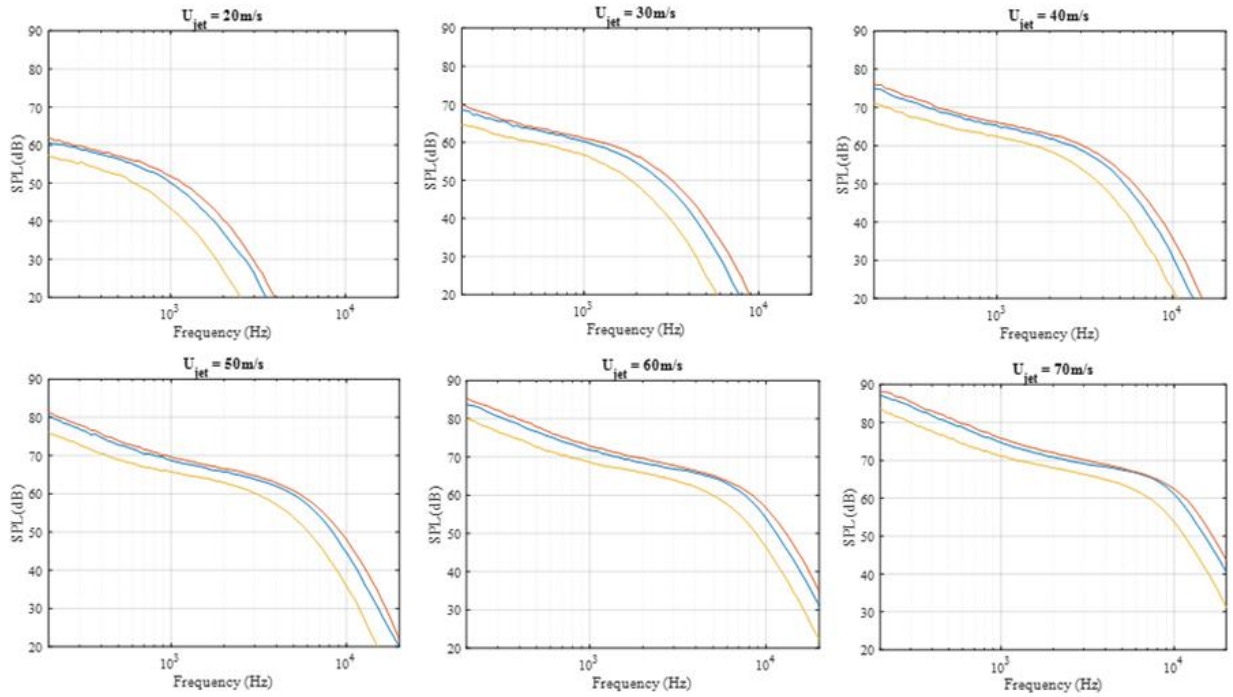

Fig. 20: *Plots displaying the surface pressure fluctuation evolution in the streamwise direction at six different jet velocities. The autospectra are shown. The microphones locations are 1 (—), 2 (—), and 3 (—).*

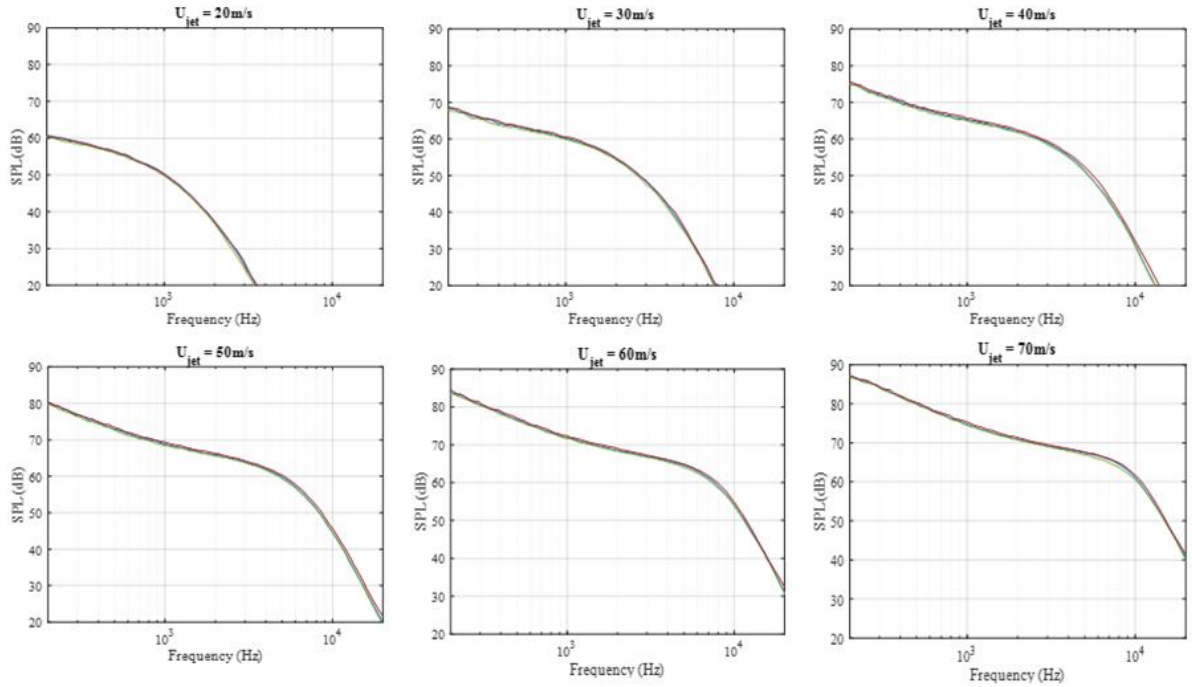

Fig. 21: *Plots displaying the surface pressure fluctuations in the spanwise direction at six different jet velocities. The autospectra are shown. The microphones locations are 4 (—), 2 (—), and 5 (—).*

C. Aerodynamic Calibration

i. Nozzle Exhaust Uniformity

In order to understand the flow close to the nozzle, pitot measurements were taken for the full range of flow speeds and at 3 varying distances from the throat. The data was taken at the nozzle half height of 6.35 mm at a sampling rate of 6400 Hz for 5 seconds. The tests were determining two characteristics of wall jet flow: the square root relationship between jet velocity and dynamic pressure defined by Bernoulli's equation, and a constant coefficient of pressure equal to one maintained streamwise in the potential core close to the nozzle. The graph in Fig. 22 shows that the flow velocity at the throat across the entire span of the nozzle diverges by no more than +/- 0.1% from the expected ½ power relationship.

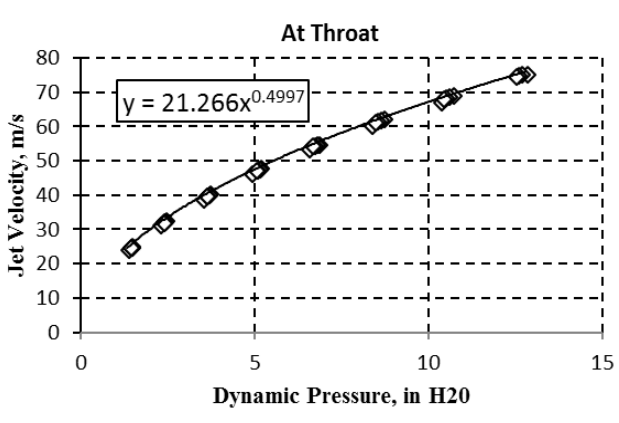

Fig. 22: *Dynamic pressure at the throat plotted against exit velocity for every point along span.*

ii. Spanwise Flow Uniformity

After initial testing, the wall jet exhibited non-uniform behavior across a significant portion of the flat plate span. Iterative testing led to increased uniformity across the span, however the results were not satisfactory. Ultimately, testing led to the conclusion that the boundary layer at the nozzle exit remained laminar rather than separating uniformly. After identifying this, a 0.5 mm thick strip of serrated tape was added in the contraction chamber resulting in the desired flow characteristics. The magnitude of the local flow velocity, flow symmetry near the centerline, and spanwise distance of uniform behavior all match comparably to the behavior of the original anechoic wall jet tunnel. Preliminary results are plotted in Fig. 23.

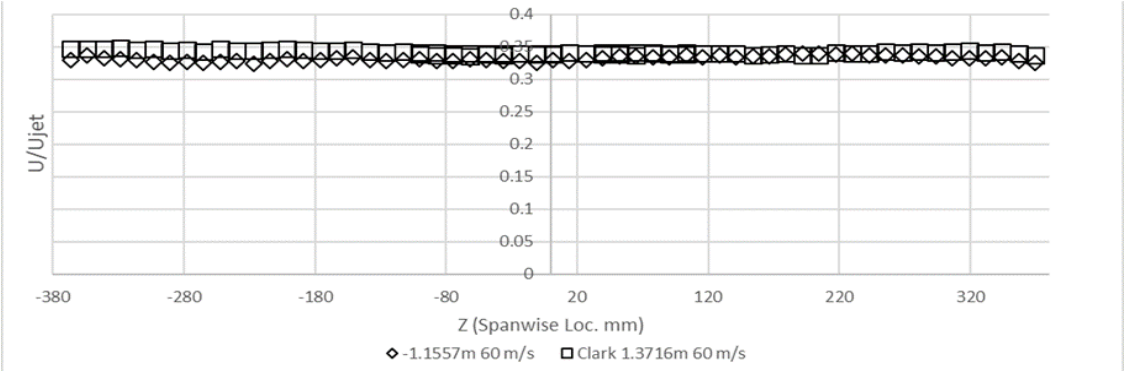

Fig. 23: *Spanwise uniformity comparison from -381mm to 381mm for the new facility vs the data from Clark (2014) in the old wall jet. The test plate extends 304.8 mm from either side of the centerline.*

After discovering that the spanwise uniformity improved greatly with the installation of a 0.5mm thick strip of serrated tape just before the nozzle exit, a more robust sharp corner was developed and installed. Further measurements were taken to determine the spanwise uniformity of the flow. This performance metric is important, because it ensures a smooth, continuous flow over the planar testing area and ensures that the entire width of the testing area is exposed to the same conditions. Figure 24 displays the spanwise nature of the flow across the z direction under different testing conditions. The spanwise distance from the centerline ($z = 0$) is displayed on the abscissa, while the local mean velocity normalized on the nozzle exit velocity is shown on the ordinate. For the new facility, spanwise checks were performed at the leading and trailing edges of the test plate, located at $x/h = 89$ and $x/h = 137$ respectively. These locations were selected because they characterize the inflow and outflow planes of the testing area. The wall normal position of $y/h = 1$ was chosen because it occurs in the U_m regime and is most likely to have uniformity. The nozzle exit velocity was $U_{jet} = 70\ m/s$. A third set of data is also plotted in Fig. 24, which represents a spanwise uniformity check performed in the old facility by Clark (2015). Although the experimental conditions differ for this test, $y/h = 0.5$ and $U_{jet} = 60\ m/s$, it remains important as a baseline comparison. All datasets remain relatively level through the test plate area ($-305mm < z < 305mm$), with the highest deviations occurring at

$U/U_{jet} = \pm 0.025$ for the leading edge case in the new facility. The edges of the flow are visible at around 400mm from the center line. This is indicated by the sudden decrease in local velocity for all datasets. The leading edge and trailing edge runs in the new facility are separated by a distance of $U/U_{jet} = 0.07$. This signifies the flow decay across the test area in the streamwise direction. The spanwise flow from the old facility is the most level, with a standard deviation of 0.0027 over the testing plate region. The standard deviations of the leading edge and trailing edge runs for the new facility are 0.0057 and 0.0064 respectively. Even though the new facility's values are larger, they are only marginally so when compared to the maximum U/U_{jet} value of 0.4. Additionally, the differing test conditions cause some uncertainty with these comparisons. However, relatively small deviations in the data yield an acceptable performance of the new facility's spanwise flow uniformity.

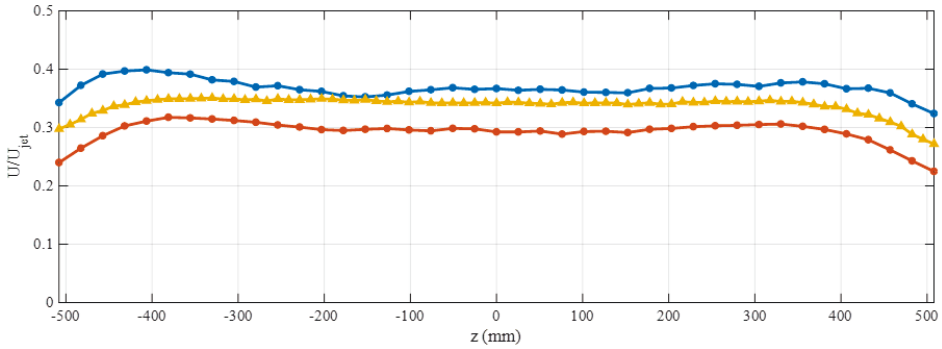

Fig. 24: *Spanwise uniformity of the flow, where (●) was taken at y/h = 1, x/h = 89, and U_{jet} = 70m/s; (●) was taken at y/h = 1, x/h = 137, and U_{jet} = 70m/s; (▲) is from the old facility, taken at y/h = 0.5, x/h = 108, and U_{jet} = 60m/s.*

Cross-sectional measurements of the flow field were also conducted at $x/h = 89$ and $x/h = 137$, Fig. 25. Each run was taken at $U_{jet} = 70\ m/s$. The contours are of local mean velocity normalized on the nozzle exit velocity. The plots show the spanwise uniformity in the horizontal direction and the boundary layer profile in the vertical. There is significant decay in the cross-sectional structure of the flow over the test plate including a reduction in the width of the region of two-dimensional flow and in the maximum velocity, which reduces from $U/U_{jet} = 0.35$ to $U/U_{jet} = 0.30$ approximately. The plots also show the wall jet boundary layer and shear layer growth. For example, the $U/U_{jet} = 0.20$ contour occurs at $y = 75\ mm$ before the test section and moves to $y = 100\ mm$ after the test section. Interestingly, two pockets of higher speed air can be seen on the spanwise edges of each cross-section. It is likely that these arise from the nozzle end effects. Although they disrupt the spanwise uniformity of the flow, their location is outside of the test plate.

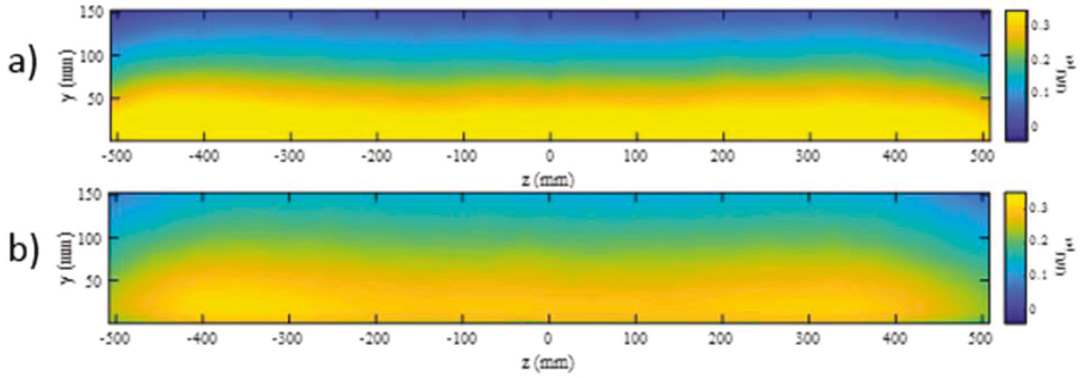

Fig. 25: *Cross sectional measurements of the flow's mean velocity profile taken at $U_{jet} = 70\ m/s$. Plot a) occurs at $x/h = 89$, and plot b) occurs at $x/h = 137$.*

iii. Centerline Boundary Layer Profiles

Vertical boundary layer profiles were at streamwise locations of 0.9779 m, 1.1557 m, 1.3081 m, 1.4605 m, and 1.7653 m downstream of the nozzle and for flow speeds at the nozzle of 30, 40, 50, 60, and 70 m/s. The measured boundary layer profiles normalized on boundary layer thickness and maximum velocity are shown in Fig. 26. The profiles are also shown normalized on maximum velocity and the quantity $y_{1/2}$, which is defined as the vertical distance from the wall to the point where the local velocity decays to half the maximum value in the outer region of the boundary layer. From Fig. 26, the assertion that the profiles are self-similar when normalized becomes evident. Normalization of the vertical distance on the boundary layer thickness leads to excellent collapse of the data in the inner region of the boundary layer. Normalization on $y_{1/2}$ improves the collapse of the data in the outer region while increasing the scatter of the data in the inner region slightly.

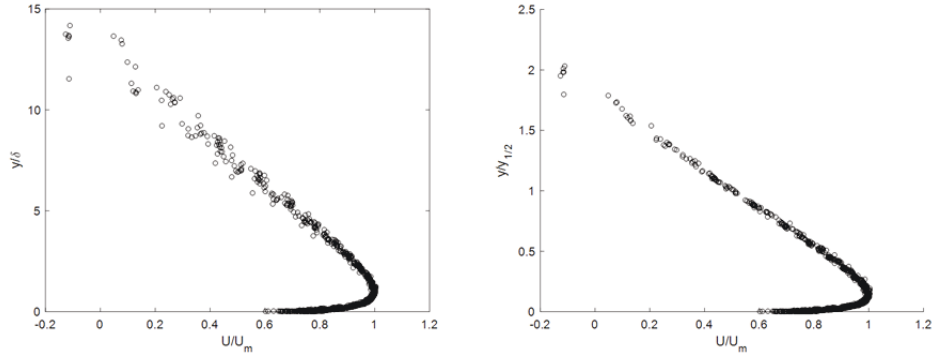

Fig. 26: *All measured boundary layer profiles normalized on maximum velocity and boundary layer thickness (a) and $y_{1/2}$ (b)*

Before an analysis could be conducted to characterize the flow everywhere in the facility, the boundary layer parameters were first extracted from each profile. First, a reference profile was chosen from the data set that presented the least amount of scatter, particularly near the location of maximum velocity. For this analysis, the reference profile chosen was measured at a streamwise location of 2044.7 mm with a jet speed of 40 m/s, shown in Fig. 27. Throughout the data collection process, each boundary layer profile was plotted in this manner to assess the quality of each profile and identify any sources of error or uncertainty. One of the common factors that lead to poor quality profiles during early testing was uncertainty in understanding the precise location of the pitot probe at the wall. In this analysis, it is critical that the probe starts as close to the wall as physically possible, while measuring as many data points as close to the wall as possible. It was for this reason an electrical circuit was implemented to detect precise contact between the probe and the wall. Knowing that the location of the probe was of critical importance, uncertainty in the position of each data set was determined using a secondary analysis. This analysis involved backing out the true position of the probe near the wall using the theoretical y+ values calculated for the given flow parameters based on George et al (2000). Also, in order to correct for any instrumentation error due to the traverse, further correction of the probe position was performed based on the actual pitch of the motors.

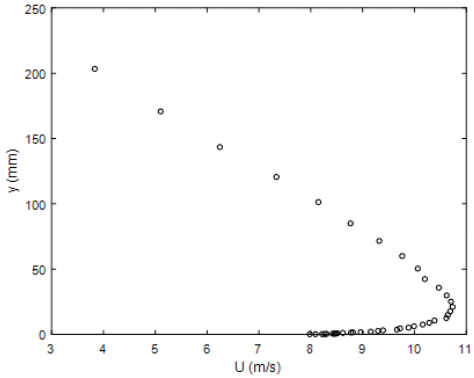

Fig. 27: *Reference profile obtained at 2044.7 mm downstream of the nozzle with a jet velocity of 40 m/s*

After collecting all profiles and qualitatively determining a reference profile, the boundary layer thickness of the reference profile was then input as the location of the maximum velocity. A curve fit was then applied which approximated the profile close to the wall as a function of velocity raised to a variable power. This curve fit was used to extrapolate the data points closest to the wall in order to determine the integral thickness using the following relations:

$$\delta^* = \int_0^{\delta}(1-\frac{U}{U_m})dy \tag{4.1}$$

$$\theta = \int_0^{\delta}(1-\frac{U}{U_m})\frac{U}{U_m}dy \tag{4.2}$$

Here δ^* is the displacement thickness, θ is the momentum thickness, δ is the boundary layer thickness, U is the local velocity at a point in the boundary layer, and U_m is the maximum velocity in the boundary layer. These integrals were evaluated numerically using the data collected by the pitot probe for each profile and the extrapolated data near the wall. An in-house MATLAB program was developed to assist in performing this analysis for all the boundary layer profiles measured, producing the results in Table 1.

Table 1: *All boundary layer parameters obtained from the measured profiles*

Run	X (in)	X (mm)	Ujet	Re	Tf (K)	Uref (m/s)	Um (m/s)	Delta (mm)	eltastar (mm	Theta (mm	Rem	Rej	Rex	Cf	yhalf (mm)
1	45.5	1155.7	20	31250.34	294.4833	20.17286	6.476414	13.73701	1.063725	0.840384	5426.008	15625.17	1390640	0.006586	99.2
2	45.5	1155.7	30	46830.28	294.4833	30.2301	10.35296	12.5679	0.837399	0.708687	7935.613	23415.14	2083948	0.006146	94.30588235
3	45.5	1155.7	40	62327.91	294.4833	40.2342	14.13976	12.3368	0.703991	0.600364	10638.94	31163.95	2773592	0.005827	90.91764706
4	45.5	1155.7	50	77818.91	294.4833	50.23402	18.02733	11.48686	0.708594	0.609463	12629.5	38909.45	3462941	0.005648	87.90588235
5	45.5	1155.7	60	93314.1	294.4833	60.23654	21.82668	11.3305	0.688917	0.594781	15083.08	46657.05	4152477	0.005468	88.28235294
6	45.5	1155.7	70	108686.3	294.4833	70.1597	25.63212	11.16822	0.677227	0.586566	17459.1	54343.17	4836542	0.005324	85.27058824
7	38.5	977.9	20	31263.18	294.7056	20.00273	7.031379	13.22464	0.931538	0.763141	5721.824	15631.59	1203632	0.006523	84.89411765
8	38.5	977.9	30	46816.14	294.7056	29.95379	11.11551	11.08594	0.907005	0.747257	7582.494	23408.07	1802421	0.006197	78.11764706
9	38.5	977.9	40	62979.06	294.7056	40.32179	15.41935	11.19173	0.827127	0.692477	10611.73	31489.53	2424694	0.005829	76.98823529
10	38.5	977.9	50	78292.07	294.7056	50.1258	19.32382	11.25916	0.746832	0.634648	13378.94	39146.04	3014245	0.005589	76.98823529
11	38.5	977.9	60	93993.26	294.7056	60.17835	23.39144	11.1462	0.775258	0.658542	16032.7	46996.63	3618741	0.005408	75.85882353
12	38.5	977.9	70	109663.6	294.7056	70.32745	27.6148	10.76404	0.743562	0.630193	18248.26	54831.82	4222050	0.005282	75.10588235
13	55.5	1409.7	20	31549.79	294.9833	20.2116	5.899215	16.72644	0.973947	0.832018	6064.009	15774.9	1751014	0.006454	124.0470588
14	55.5	1409.7	30	46563.31	294.9833	29.86912	9.104585	16.37137	0.930537	0.806039	9148.141	23281.66	2584264	0.005989	113.8823529
15	55.5	1409.7	40	62736.38	294.9833	40.28915	12.69852	14.40732	0.842847	0.727442	11215.9	31368.19	3481869	0.005771	113.5058824
16	55.5	1409.7	50	78088.24	295.65	50.26391	15.99293	14.69871	0.812276	0.704313	14378.15	39044.12	4333897	0.005516	110.4941176
17	55.5	1409.7	60	93533.27	295.65	60.20558	19.30396	14.73185	0.829854	0.714228	17393.99	46766.64	5191097	0.005328	110.1176471
18	55.5	1409.7	70	108855.9	295.65	70.10402	22.83442	14.47936	0.867096	0.741028	20212.26	54427.96	6041503	0.005184	108.9882353
19	68.5	1739.9	20	31025.75	295.2611	19.97857	5.305939	22.8191	1.411213	1.132069	7402.612	15512.88	2125264	0.006224	147.3882353
20	68.5	1739.9	30	46522.65	295.4833	29.97497	8.380605	19.83103	1.211356	1.001645	10155.3	23261.33	3186802	0.005876	142.1176471
21	68.5	1739.9	40	62157.02	295.4833	40.04834	11.52669	19.20075	1.139391	0.964486	13523.67	31078.51	4257756	0.005578	139.4823529
22	68.5	1739.9	50	77585.58	295.4833	49.98911	14.59658	18.66044	1.138256	0.958368	16643.51	38792.79	5314612	0.005371	137.9764706
23	68.5	1739.9	60	92997.45	295.4833	59.91912	17.69964	18.77454	1.127483	0.950326	20305.13	46498.73	6370325	0.00518	139.4823529
24	68.5	1739.9	70	108589.1	295.4833	69.96498	20.92	18.4803	1.12587	0.946523	23623.42	54294.56	7438355	0.005039	135.3411765
25	80.5	2044.7	20	31530.11	294.8722	20.04364	4.980138	24.45337	1.474798	1.209767	7542.154	15765.06	2538174	0.006203	174.4117647
26	80.5	2044.7	30	47019.15	295.0389	29.94671	7.734938	22.03306	1.481814	1.252909	10534.74	23509.58	3785042	0.005837	166.7647059
27	80.5	2044.7	40	63105.14	295.3167	40.23099	10.74314	20.95032	1.17242	1.013806	13899.28	31552.57	5079964	0.00555	163.8235294
28	80.5	2044.7	50	78124.94	294.3167	49.93581	13.42551	22.43099	1.440822	1.205686	18549.12	39062.47	6289058	0.005266	164.1176471
29	80.5	2044.7	60	93843.78	294.3167	59.98296	16.19135	22.73636	1.431103	1.192077	22675.04	46921.89	7554424	0.005077	161.5764706
30	80.5	2044.7	70	109313.5	294.3167	69.87087	19.12751	20.65706	1.370929	1.141143	24337.21	54656.74	8799735	0.005012	158.6117647

Once these parameters were derived, it was necessary to fit the data to the power-law relations of Wygnanski *et al.* (1992). These relations take the form:

$$\frac{U_m}{U_o} = A_U Re_j^{n+1} Re_x^n \tag{4.3}$$

$$\frac{\delta^*}{b} = A_D Re_j^{p-2} Re_x^p \tag{4.4}$$

$$\frac{y_{1/2}}{b} = A_y Re_j^{m-2} Re_x^m \tag{4.5}$$

$$\delta = A\delta^* \tag{4.6}$$

$$\theta = B\delta^* \tag{4.7}$$

In these relations U_o is the jet velocity, A_U, A_D, A_y, A, and B are constants to be determined. Re_j is the Reynolds number based on jet velocity and nozzle height, Re_x is the Reynolds number based on jet velocity and distance to the measurement location, b is the nozzle height, and n, m, and p are power-law constants to be determined. From the data collected with the flattened pitot probe, experimental values can be used in the above relations for all variables except for the 5 constants and the 3 power-law constants. By considering all boundary layer profiles with different streamwise locations and flow speeds, a best fit (method of least squares) algorithm was used to approximate the 5 constants and 3 power-law constants. These results are given for this analysis in Table 2.

Table 2: *Power-law constants which characterize the flow parameters in the Wall-Jet Tunnel*

A_U	**1.497**
A_D	**0.0049**
A_Y	**0.1972**
A	**16.012**
B	**0.8387**
n	**-0.4684**
p	**0.9232**
m	**0.9649**

Utilizing these relations, U_m, δ^*, $y_{1/2}$, δ, and θ can all be calculated for a given jet velocity and dimensions of the wall jet facility. A comparison of the calculated values (ordinate) for U_m, δ^*, $y_{1/2}$, δ, and θ with the measured values (abscissa) at each measurement point is given in Figure 28. The diagonal line represents the line of perfect fit and has a slope of one. These figures show that the least error occurs for the maximum velocity and half-height curve fits. The boundary layer parameters show significantly more scatter and are much more sensitive to experimental conditions.

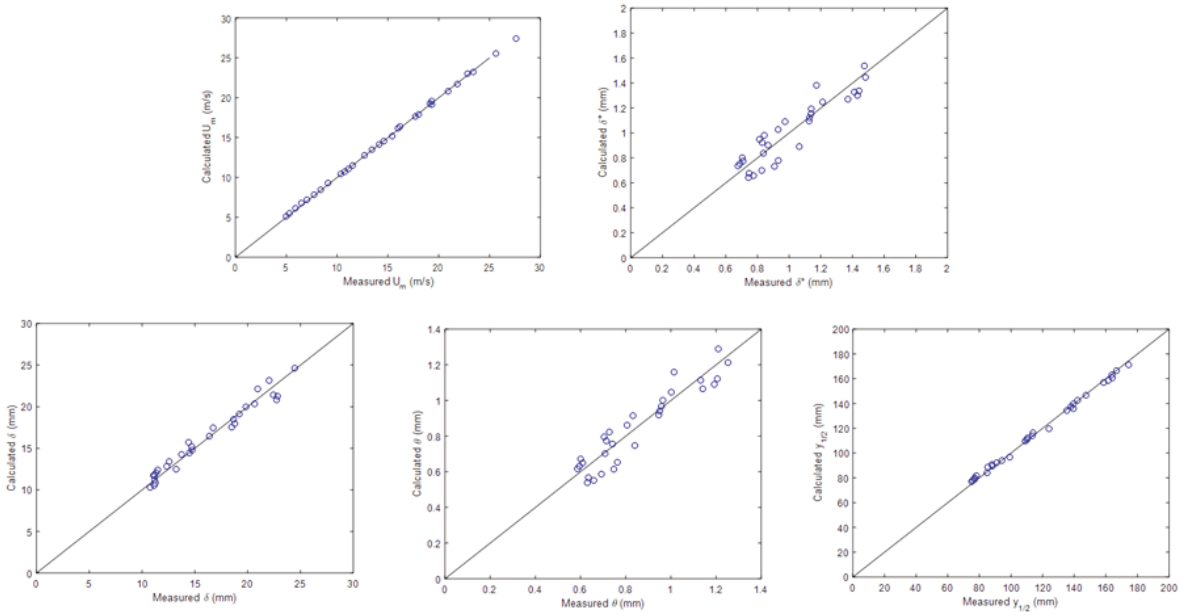

Figure 28: *(a) Comparison of measured values of U_m to those calculated using the power-law constants above. (b) Comparison of measured values of δ^* to those calculated using the power-law constants above. (c) Comparison of measured values of δ to those calculated using the power-law constants above. (d) Comparison of measured values of θ to those calculated using the power-law constants above. (e) Comparison of measured values of $y_{1/2}$ to those calculated using the power-law constants above.*

V. Conclusion

The detailed design and calibration of a new Anechoic Wall Jet wind tunnel has been presented. The tunnel is based on the old wall jet facility at Virginia Tech with a modified anechoic chamber, contraction section and settling chamber. Significant design considerations include a much larger anechoic chamber in order to enable movement and more room for instrumentation, modified nozzle to improve separation of the flow, inclusion of a full contraction slope in the contraction chamber and an optimized settling chamber to straighten and reduce the upstream acoustics from influencing the wall-jet flow.

Acoustic and aerodynamic calibrations were performed to analyze the facility for flow speeds from 20 m/s to 70 m/s. The primary purpose of the calibrations was to characterize the noise produced by the flow over various surfaces and edges. Far-field testing using a streamwise array of half-inch B&K microphones was performed for varying flow speeds to determine the background noise in the facility. A study of the far-field acoustics with varying observer distance was also performed. These studies showed lower sound pressure levels for frequencies up to 700 Hz compared to the old facility, making the tunnel ideal for low frequency research. At higher frequencies, an increase in the sound levels is observed; however, the results are not significantly different compared to the old facility. Surface pressure fluctuations were measured using Sennheiser microphones to indicate the spanwise uniformity in the turbulence levels of the flow. Streamwise decay in the energy levels can be observed in the autocorrelation plots at various streamwise locations.

Aerodynamic calibrations were performed to assess the quality of the flow. Various mean velocity measurements taken at different streamwise cross-sections and spanwise profiles indicate that the incoming flow is uniform. Increase in the cross-sectional spread of the flow with downstream distance was clearly observed in the streamwise cross-sectional profiles. Boundary layer profiles along the centerline were measured and suitable algorithms were used to calculate the boundary layer parameters given by U_m, δ^*, $y_{1/2}$, δ, and θ for a given jet velocity and dimensions of the wall jet facility parameters. Various corrections to reduce uncertainties have been incorporated in the above study. For future experiments, particular attention must be paid to the pitot probe positioning close to the wall. Additionally, increasing the number of measurement points near the wall and including more data sets at various streamwise locations can be done for further reduction in experimental uncertainties.

VI. Acknowledgements

The authors would like to acknowledge the Office of Naval research, in particular Debbie Nalchajian and Mark Spector, for their support under grant N00014-18-1-2179. The support of the National Science Foundation, in particular Ron Joslin, under grant CBET-1802915 is also acknowledged.

References

Alexander, N. and W. Devenport (2015). Noise Produced by Fabric and Wire Mesh Covered Panels in Low-Speed Anechoic Wind Tunnels. Aviation 2015. Dallas, TX.

Alexander, W. N. (2009). Normalization of roughness noise on the near-field wall pressure spectrum. MS, Virginia Polytechnic Institute and State University.

Alexander, W. N. (2011). Sound from Rough Wall Boundary Layers. PhD, Virginia Polytechnic Institute and State University.

Alexander, W. N. and W. J. Devenport (2014). Noise from Boundary Layer Flow over Fabric Covered Perforate Panels. 20th AIAA/CEAS Aeroacoustics Conference. Atlanta, GA.

Alexander, W. N., W. J. Devenport and S. A. L. Glegg (2013). "Predictions of Sound from Rough Wall Boundary Layers." AIAA Journal **51**(2): 465-475.

Alexander, W. N., W. J. Devenport and S. A. L. Glegg (2014). "Predictive Limits of Acoustic Diffraction Theory for Rough Wall Flows." AIAA Journal **52**(3): 634-642.

Awasthi, M. (2012). High Reynolds Number Turbulent Boundary Layer Flow over Small Forward Facing Steps. MS, Virginia Polytechnic Institute and State University.

Awasthi, M. (2015). Sound Radiated from Turbulent Flow over Two and Three-Dimensional Surface Discontinuities. PhD, Virginia Tech.

Awasthi, M., B. Bryan, W. Devenport and S. Glegg (2013). Sound Radiation from Rounded Steps and Gaps. 19th AIAA/CEAS Aeroacoustics Conference. Berlin.

Awasthi, M., W. J. Devenport, T. W. Meyers, W. N. Alexander and S. A. Glegg (2014). Aeroacoustics of 2D and 3D Surface Discontinuities. 20th AIAA/CEAS Aeroacoustics Conference. Atlanta, GA.

Catlett, M., W. J. Devenport and S. Glegg (2014). "Sound from boundary layer flow over steps and gaps." Journal of Sound and Vibration **333**: 4170-4186.
Catlett, M. R. (2010). Flow induced noise from turbulent flow over steps and gaps. MS, Virginia Polytechnic Institute and State University.
Clark, I. A. (2017). Bio-Inspired Control of Roughness and Trailing Edge Noise. PhD PhD, Virginia Tech.
Clark, I. A. (2014). A Study of Bio-Inspired Canopies for the Reduction of Roughness noise. *Master of Science Thesis.* Blacksburg. Virginia Polytechnic Institute and State University.
Clark, I. A., C. A. Daly, W. Devenport, W. N. Alexander, N. Peake, J. W. Jaworski and S. Glegg (2016). "Bio-inspired canopies for the reduction of roughness noise." Journal of Sound and Vibration **385**: 33-54.
Clark, I. A., W. J. Devenport, J. W. Jaworski, C. Daly, N. Peake and S. Glegg (2014). The Noise Generating and Suppressing Characteristics of Bio-Inspired Rough Surfaces. AIAA/CEAS 20th Aeroacoustics Conference. Atlanta, GA.
Devenport, W., N. Alexander, S. Glegg and M. Wang (2018). "The Sound of Flow Over Rigid Walls." Annual Review of Fluid Mechanics **50**(1): 435-458.
Devenport, W., E. A. Wahl, S. A. L. Glegg, W. Nathan Alexander and D. L. Grissom (2010). "Measuring surface pressure with far field acoustics." Journal of Sound and Vibration **329**(19): 3958-3971.
Devenport, W. J., D. L. Grissom, W. Nathan Alexander, B. S. Smith and S. A. L. Glegg (2011). "Measurements of roughness noise." Journal of Sound and Vibration **330**(17): 4250-4273.
Fang, Fuh-min, Chen, J.C., Hong, Y.T. (2001). Experimental and analytical evaluation of flow in a square-to-square wind tunnel contraction, *Journal of Wind Engineering and Industrial Aerodynamics,* vol. 89, pg. 247-262.
George, W., Abrahamsson, H., Eriksson, J., Karlsson, R., Löfdahl, L., & Wosnik, M. (2000). A similarity theory for the turbulent plane wall jet without external stream. Journal of Fluid Mechanics*, 425*, 367-411.
Glegg, S. and W. Devenport (2009). "The far-field sound from rough-wall boundary layers." Proceedings of the Royal Society A: Mathematical, Physical and Engineering Sciences **465**(2106): 1717-1734.
Grissom, D. L. (2007). A study of sound generated by a turbulent wall jet flow over rough surfaces. PhD, Virginia Polytechnic Institute and State University.
Jacob, M. C., A. Louisot and D. Juve (2001). "Experimental Study of Sound Generated by Backward-Facing Steps under Wall Jet." AIAA Journal **39**(7): 1254-1260.
Smith, B. S. (2008). Wall jet boundary layer flows over smooth and rough surfaces. PhD, Virginia Polytechnic Institute and State University.
Wygnanski, I., Katz, Y., Horev, E. (1992). “On the applicability of various scaling laws to the turbulent wall jet,” *Journal of Fluid Mechanics, 234,* 660-690.